

Stephenson 2 DFK 52: Discovery of an exotic red supergiant in the massive stellar cluster RSGC2

M. A. Siebert¹, E. De Beck¹, G. Quintana-Lacaci², and W. Vlemmings¹

¹ Department of Space, Earth and Environment, Chalmers University of Technology, Gothenburg, Sweden

² Department of Molecular Astrophysics, Instituto de Física Fundamental, Madrid, Spain

Accepted July 6, 2025

ABSTRACT

Atacama Large Millimeter/submillimeter Array (ALMA) observations at 1.3mm have recently revealed surprising complexity in the circumstellar environment of DFK 52, a red supergiant (RSG) located in the Stephenson 2 massive open cluster. We provide an initial characterisation of the star's mass-loss properties by studying its circumstellar emission in continuum, ¹²CO, ¹³CO, and SiO rotational lines. We find that DFK 52 is surrounded by an extremely large outflow (up to 50,000 au in radius) that shows complex morphologies in both its molecular and dust emission. The size of the circumstellar medium is unprecedented, even when compared with other known extreme RSGs, and its lower luminosity indicates that its mass ejection mechanism may be unique among this population. The molecular emission can be partially reproduced by a two-component model consisting of a fast (27 km s⁻¹) detached equatorial component with $\dot{M} \sim 0.05 M_{\odot}$ and a slow (10 km s⁻¹) spherical envelope with $\dot{M} \sim 3 \times 10^{-6} M_{\odot} \text{ yr}^{-1}$. This suggests that DFK 52 underwent a dramatic mass-loss event ~ 4000 years ago, but has since transitioned into having a slower more symmetric mass loss. We conservatively estimate a total mass of $0.1 - 1 M_{\odot}$ in the complex extended regions of the outflow. The uncertain nature of the dramatic mass loss warrants extensive follow-up of this likely supernova progenitor.

Key words. Stars: supergiants, Stars: mass-loss, Stars: circumstellar matter, Stars: evolution

1. Introduction

The mass loss of red supergiants (RSGs) is critical to their evolution and to the observed characteristics of Type II-p supernovae (SNe). The efficiency of these winds for the duration of the RSG phase can determine the amount of hydrogen stripped from the star, the density of interacting dust at the time of explosion, and the structure of SN remnants. Among well-studied RSGs, a morphological distinction has emerged between those exhibiting slower, traditional, approximately spherical mass loss (e.g. α Ori, α Sco; $10^{-7} - 10^{-6} M_{\odot} \text{ yr}^{-1}$) and more luminous extreme RSGs, which show asymmetric outflows and mass-loss rates of order $10^{-4} M_{\odot} \text{ yr}^{-1}$ (e.g. VY CMa, NML Cyg, VX Sgr). Neither the underlying physical mechanisms that produce these exotic objects nor their ubiquity among the red supergiant population is understood, despite their major relevance to evolutionary models of massive stars and core-collapse SNe.

Stephenson 2 (RSGC2) is a massive cluster of at least 26 RSGs located at the base of the Scutum-Crux spiral arm at a distance of $5.8^{+1.91}_{-0.76}$ kpc (Davies et al. 2007). It has been inferred that this was a site of recent starburst activity in the region where the arm intersects the galactic bulge. Humphreys et al. (2020) investigated the mass-loss properties of cluster members from dust emission in their mid-infrared (IR) spectral energy distributions (SEDs), and noted its wide spread in luminosities, initial masses, and mass-loss rates when compared to other RSG clusters.

In these previous studies, the source DFK 52 appears as a rather ordinary RSG in the cluster. Its radial velocity and plane-of-sky position place it in the centre of RSGC2, the strength of its CO absorption band in the near-IR implies an M0-type supergiant (Davies et al. 2007), and its estimated luminosity ($2 \times 10^4 L_{\odot}$) is typical, though on the low end for RSGs. How-

ever, Humphreys et al. (2020) noted that its *J*-band flux is too low to be reproduced with a stellar model and the average reddening factor for the cluster. This could either arise from variable line-of-sight extinction from the intervening interstellar medium (ISM), or from circumstellar dust.

In this letter we report the discovery of a surprising circumstellar environment toward DFK 52 based on recent observations with ALMA. Through its molecular line and continuum emission at millimetre wavelengths, we present the kinematics and spatial distribution of gas and dust surrounding this star, and compare them with other known extreme RSGs. With these constraints, we aim to provide starting insights into the evolutionary status and the mass-loss history of DFK 52 that will serve as a basis for future more detailed studies of this unique object.

2. Observations

The millimetre-wavelength observations of DFK 52 were conducted as part of two ALMA programmes. The first (2023.1.01519.S) covered a sample of 13 RSGs in RSGC2. These observations were performed with two configurations of the main 12m array using the Band 6 receiver (Ediss et al. 2004), achieving a spatial resolution of $0.35''$ at 230 GHz and a maximum recoverable scale (MRS) of $12.5''$. Four spectral windows were positioned in the 214 – 233 GHz range targeting ¹²CO $J = 2 - 1$ at 230.538 GHz and SiO $J = 5 - 4$ at 215.596 GHz. The spectral resolution is 1.27 km s^{-1} , and the total bandwidth is 1.8 GHz. The follow-up project (2024.A.00018.S) targeted only DFK 52 with the Atacama Compact Array (ACA) to recover all of the extended emission. The spectral set-up for the ACA matches the resolution and line coverage of the 12m data, with the addition of the ¹³CO $J = 2 - 1$ transition at 220.399 GHz.

Observations for both ALMA projects were reduced with the standard ALMA calibration pipeline (Hunter et al. 2023), and visibilities from different configurations were combined in the uv -plane with antenna-specific weighting. Continuum subtraction was performed in the visibility plane, and imaging was done with the CASA task `tclean` using Briggs weighting and a robust parameter of 0.5. The final brightness sensitivities are 1 mJy/beam for spectral line data and 20 μ Jy/beam for the continuum. A common feature across all ALMA observations of RSGC2 was a significant amount of contamination from the interstellar medium (ISM) in CO. To reduce its impact on our results, we identified the channels where ISM emission or absorption spatially overlaps with circumstellar CO, and did not consider them in our analysis. For continuum maps, line-free channels were used in the imaging process, and the ^{12}CO spectral window was omitted entirely to ensure the ISM was excluded. Comparing images created with and without the supplementary ACA data, the total flux recovery is $\sim 100\%$ for spectral lines and 80% for the continuum in the main-array dataset.

3. Analysis and results

3.1. Continuum

The 1.3 mm continuum toward DFK 52 is shown in Fig. 1. We observed emission in a variety of substructures, including a very low-brightness ($\sim 1\text{--}3\sigma$ unsmoothed) extended component that is elongated in the N–S direction and reaches a maximum radius of $8''$. At shorter radii, more compact components are present, including two bright clumps in the NW and E directions (labelled A and B), and an arc structure to the SW (labelled C). Together, these structures account for $\sim 15\%$ of the total flux. Notably, no centrally peaked continuum source is found at the position of the star (measured by unresolved SiO emission; Section 3.2). The total continuum flux is 17.2 ± 1.7 mJy.

The continuum map appears similarly complex in shape to the extreme RSG VY CMa, where the millimetre emission is dominated by thermal radiation from asymmetrically ejected dust clumps (Kamiński 2019). However, the surrounding VY CMa are observed at projected distances of 250 – 800 au (see clumps ‘A–D’ in Humphreys et al. 2024), whereas the A and B clumps around DFK 52 are found at 5,800 and 12,000 au, and the extended emission reaches a distance of $\sim 50,000$ au (assuming the cluster distance of 5.8 kpc; see Appendix D). Following the methods of O’Gorman et al. (2015) and De Beck et al. (2025) for VY CMa and NML Cyg and using a dust grain emissivity of $\beta = 0.9$, we derive dust temperatures $T_A \approx 102 \pm 9$ K, $T_B \approx 76 \pm 7$ K, and $T_C \approx 63 \pm 6$ K, and dust mass estimates $M_A \approx (1.7 \pm 0.36) \times 10^{-4} M_\odot$, $M_B \approx (1.1 \pm 0.24) \times 10^{-4} M_\odot$, and $M_C \approx (4.4 \pm 0.95) \times 10^{-4} M_\odot$. This assumes that the A, B, and C continuum components are situated at offsets of $\Delta_A \approx 1.0''$, $\Delta_B \approx 2.1''$, and $\Delta_C \approx 3.2''$ in the plane of the sky and that their emission is optically thin. These masses are comparable to the estimates for continuum dust clumps around VY CMa, which have $M \sim 10^{-4} M_\odot$ (Humphreys & Jones 2022).

Adding to the peculiarity of the continuum map, the spectral energy distribution (SED) shows a clear double-peaked shape (Appendix A.1). This is different from VY CMa and NML Cyg, whose SEDs exhibit much higher fluxes in the mid-IR contributed by significantly warmer dust found close to the star (Kamiński 2019; Justtanont et al. 1996). Considering the large physical scales in the ALMA image, the secondary peak in the SED, and the lack of mid-IR excess or millimetre emission at the stellar position, we suggest that the dust emission is dominated

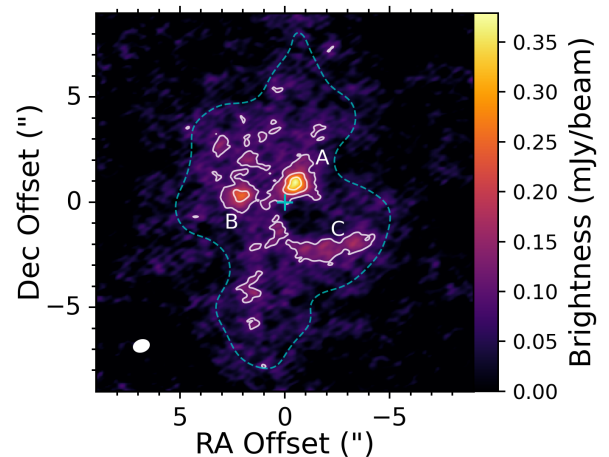


Fig. 1. 220 GHz continuum toward DFK 52. The stellar position (see Section 3.2) is marked with a blue cross, and the A, B, and C components are labelled. The white contours are shown at $[5, 10, 15]\sigma$, and the dashed blue contour represents 3σ for the image residuals after smoothing to a $2''$ resolution, tracing the low-brightness extended component.

by a cold detached component. Using the same method as before, but for the total ALMA flux, and adopting an average dust temperature of 50 K (inferred from the far-IR SED peak). This gives $M_d \approx (6.6 \pm 0.7) \times 10^{-3} M_\odot$, or a total envelope mass of $1.3 M_\odot$ if a gas-to-dust ratio of 200 is assumed (Humphreys et al. 2020).

3.2. Molecular emission

The spatial and kinematic morphology of rotational line emission seen toward DFK 52 is summarised in Fig. 2. We briefly present a number of important features.

- SiO $J = 5 - 4$ is spatially unresolved, and parabolic in line shape. This is consistent with optically thick thermal emission at the stellar position, as is measured toward many AGB and RSG stars. From this, we measure the systemic velocity $v_{sys} = 109 \pm 1.2$ km s $^{-1}$ and stellar position $\alpha_{J2000} = 18^{\text{h}}39^{\text{m}}23.406^{\text{s}}$, $\delta_{J2000} = -06^{\circ}02'16.12''$.
- With a maximum radius of $\sim 7.5''$, the integrated ^{12}CO emission is significantly more extended than SiO. Moreover, the CO line width of $\Delta v_{10\%} \approx 54$ km s $^{-1}$ traces gas that moves ~ 2.5 times faster than SiO ($\Delta v_{10\%} \approx 20$ km s $^{-1}$).
- The CO morphology is highly asymmetric, containing numerous arcs, loops, and roughly linear components. We identify a bar-like structure extending along position angle $\text{PA} = 143^\circ$ and across the stellar position. No local maximum is measured at the stellar position.
- The size and orientation of the integrated CO emission are in quite good agreement with the extended continuum. The C component is traced well by ^{12}CO channel maps in the velocity range 130 – 138 km s $^{-1}$, while the southward continuum extension is seen in the range 92.5 – 98 km s $^{-1}$ (Appendix E).
- Despite these correlations, the A and B dust clumps have no counterparts in CO. This may result from the missing channels contaminated by the ISM. We also find that some CO flux extends beyond the scales of the diffuse dust emission.
- The physical radial extent of $^{12}\text{CO } J = 2 - 1$ structures is 45,000 au. This is roughly four times larger than the farthest components observed in this line for VY CMa (“NE Arc”; Singh et al. 2023) and NML Cyg (De Beck et al. 2025).

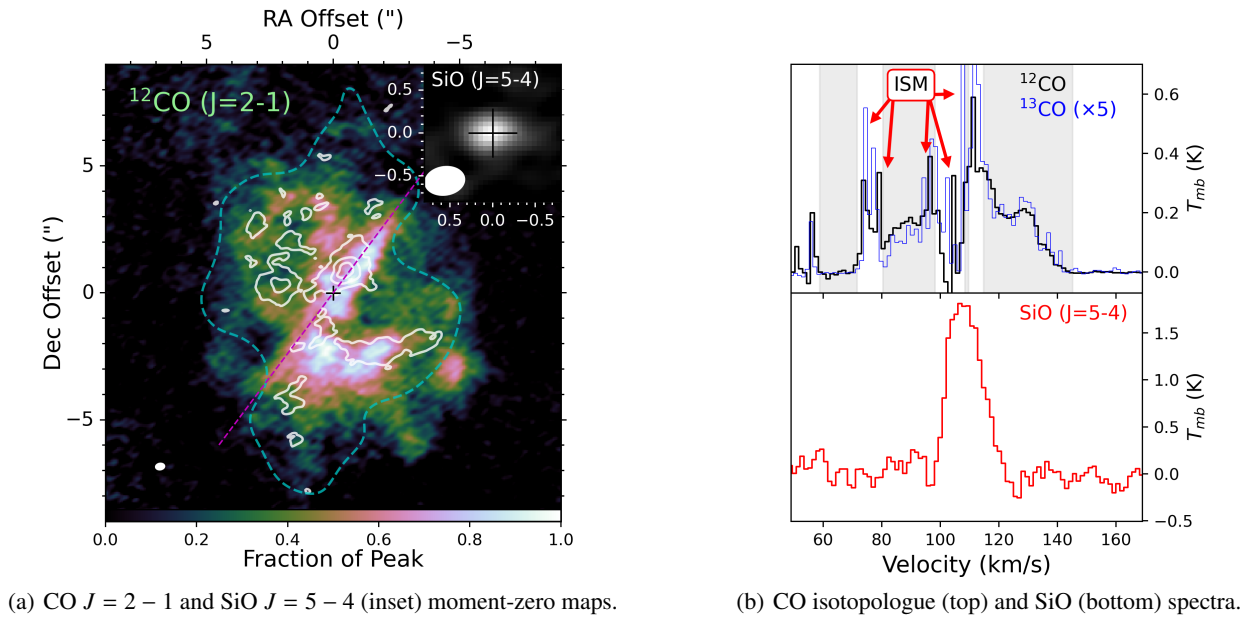


Fig. 2. Summary of molecular line emission observed toward DFK52. In the integrated CO map, the white contours denote the 220 GHz continuum emission at $[5, 10, 15]\sigma$, the blue dashed contours represent 3σ for the smoothed extended continuum component, the black cross marks the stellar position (as measured by the SiO emission peak), and the ALMA beam is displayed as a white filled ellipse in the lower right corner. The dashed magenta line in the integrated intensity map represents a line cut with $PA = 143^\circ$. Spectra were extracted taking the central pixel at the stellar position, with CO isotopologue maps first smoothed to a $15''$ beam and SiO maps at the native resolution. The grey shaded regions in the CO spectrum indicate the ISM-free channels that were used to produce the moment-zero ^{12}CO image.

Though no simple geometric prescriptions can explain the overall structure, the bar-like component in the integrated CO map (Fig. 2a) shows a significant amount of coherence across velocity space. Figure 3 shows the position-velocity (PV) diagram for ^{12}CO taken along the bar, where a shell shape is clearly seen extending to $v_{\text{sys}} \pm 27 \text{ km s}^{-1}$. This pattern suggests that the bar represents a detached disk-like structure viewed edge-on. The PV diagram also shows a bright smaller component with a total velocity width of $\sim 20 \text{ km s}^{-1}$, consistent with the SiO $J = 5 - 4$ emission. This inner structure is also seen in a perpendicular cut, suggesting that it has more 3D extent than the bar.

To estimate their physical properties, we reproduced the two components outlined above using the radiative transfer (RT) software LIne Modeling Engine (LIME 1.9.5) (Brinch & Hogerheijde 2010). The model parametrises the two structures as a slow spherically symmetric present-day mass loss, and a faster detached equatorial density enhancement (EDE) viewed edge-on (Appendix B). A model with an equatorial mass of $0.05 M_\odot$ centred at $r = 4''$ (4000 yr age) and a central component with $\dot{M} = 3 \times 10^{-6} M_\odot \text{ yr}^{-1}$ is successful at reproducing the average surface brightness and radial distribution of emission both in the compact and extended regions along the position angle of the bar structure (Fig. 3). Furthermore, the derived mass-loss rate for the slow component is in agreement with the SED modelling of warm dust performed by Humphreys et al. (2020, where a gas-to-dust ratio of 200 was adopted). However, some shortcomings of the model are clear as well. First, the blueshifted side of the torus emission is largely missing from the observational data. No combination of optical depth and excitation conditions could reproduce this, so we conclude that there is an azimuthal density asymmetry in this structure. Furthermore, there is a substantial amount of CO emission between the two components that is not captured by the model.

Because the LIME model was constructed to fit only a small fraction of the observed outflow at a specific position angle, it re-

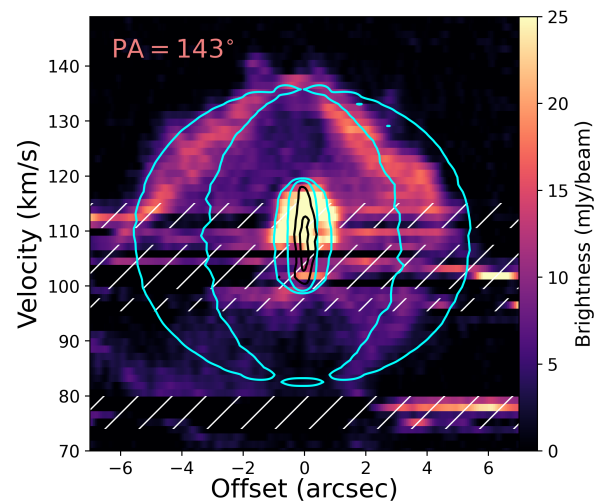


Fig. 3. PV diagram of ^{12}CO ($J = 2 - 1$) emission for a cut at $PA = 143^\circ$ with a $1''$ width. The black contours show SiO ($J = 5 - 4$) at 3σ and 10σ . The blue contours are simulated ^{12}CO ($J = 2 - 1$) emission from our two-component RT model, shown at 5 and 15 mJy/beam. The hatched regions denote velocity ranges heavily affected by ISM contamination.

produces 15% of the total line flux. Although the extended emission outside the position angle of the bar is extremely complex, we note that its velocity distribution is still quite similar to the EDE component (Appendix B). If we assume the excitation conditions of CO are common between the many extended density structures, then the model can be scaled to provide a very rough estimate of the cumulative mass in the detached high-velocity components surrounding DFK 52. Doing so offers a total mass of $\sim 0.35 M_\odot$, which is within a factor of four agreement with the estimate obtained from the continuum flux in Section 3.1.

4. Discussion

DFK 52 is a puzzling object for several reasons. The estimated physical extent of its molecular envelope is a factor of 3–4 larger than the outflows of VY CMa and NML Cyg (Singh et al. 2023; De Beck et al. 2025), and many of the irregular geometries have no clear analogues in any observed evolved star. At the same time, the luminosity is a factor of 10 lower than the known extreme RSGs (Humphreys et al. 2020), and its present-day mass loss is estimated to be two orders of magnitude smaller. We find that both the molecular line and continuum emission require a significant mass of cold material at large radii ($> 10^{17}$ cm) in the form of complex detached structures.

Given the high stellar density in the RSGC2 cluster and the strong ISM contamination in these observations, it is possible that the large-scale emission represents interactions between a stellar outflow and a quiescent local density structure in the intra-cluster medium. The maximum physical extent of the envelope is comparable to the smallest observed galactic clumps (0.1 pc; Urquhart et al. 2021), and the smooth underlying continuum emission is more similar in size and shape to molecular cloud substructures than circumstellar envelopes (Tokuda et al. 2019). However, comparison of the ^{13}CO and ^{12}CO emission across the high signal-to-noise ratio channels free of ISM contamination leads to $^{12}\text{CO}/^{13}\text{CO} \approx 5$ (Fig. 2b). This low ratio supports a stellar origin of the presented molecular emission as it requires stellar processing through the H-burning via the CNO cycle and dredge-up of the material to the surface (Boothroyd et al. 1993). We also note that none of the other sources in the RSGC2 sample show morphology anywhere similar to this, supporting the idea that the morphological complexity is connected to the star rather than to a complex intra-cluster component.

To explain the light curves of Type II SNe, it has been suggested that RSGs explode into a very dense immediate circumstellar medium (CSM), built up by a superwind ($> 10^{-3} M_{\odot} \text{ yr}^{-1}$) in the ~ 100 years prior to core collapse (Moriya et al. 2017; Davies et al. 2022). The CO emission around DFK 52 indicates that a period of dramatic mass loss with $\dot{M} > 10^{-4} M_{\odot} \text{ yr}^{-1}$ occurred ~ 4000 years ago. If we assume constant radial expansion for the disk component in the RT model, this portion of the CSM would have had a peak gas density of $n \sim 10^{10} \text{ cm}^{-3}$, or $\rho \sim 10^{-14} \text{ g cm}^{-3}$ when it was at a distance of 10^{14} cm from DFK 52, which is comparable to the pre-SN CSM density required by Yaron et al. (2017), for example. However, our analysis also suggests that this period was immediately followed by an ongoing slower mass loss with $\dot{M} \sim 3 \times 10^{-6} M_{\odot} \text{ yr}^{-1}$, and that the central gas density is lower at present. Therefore, if DFK 52 did experience a superwind, it ended without producing a SN.

Alternatively, an energetic interaction in a binary or multiple system could have contributed to the ejection of the extended material. Companion interactions and stellar mergers are known to produce bipolar, multipolar, equatorial, and complex morphologies (e.g. Lagadec et al. 2011; Olofsson et al. 2019; Kamiński et al. 2018), and common envelope evolution (CEE) is now considered to be widely responsible for rapid mass-loss events observed in AGB and post-AGB sources (Khoury et al. 2021). Furthermore, CEE in RSG systems has been invoked as an important channel to the progenitors of ultra-stripped SNe, as well as the compact binaries ($P < 1$ day) responsible for gravitational wave events (Wei et al. 2024; Klencki et al. 2021). CE ejections are known to produce expanding equatorial rings similar to the partial one seen in DFK 52 (Gómez et al. 2018), but given the lack of bipolar symmetry and the absence of any high-velocity jet components ($> 30 \text{ km s}^{-1}$), this assignment cannot be

made with the current observations. We still consider a multiple-star hypothesis to be strong here, as DFK 52's comparably low luminosity would have required an additional source of energy to drive the massive detached components (Appendix C).

5. Conclusion

We have presented resolved emission from the circumstellar environment of the red supergiant DFK 52, revealing a dusty envelope spanning unprecedented physical scales. Both the continuum and CO imply the presence of a massive ($0.1 \sim 1 M_{\odot}$) asymmetric, equatorially enhanced, detached wind expanding at $v \approx 27 \text{ km s}^{-1}$. Additionally, compact emission near the stellar position implies that the mass-loss rate and expansion velocity have dropped significantly since the ejection of this component. With the available data, a full classification of DFK 52 and its history is not yet feasible; however, we consider a short-lived superwind period or an energetic companion interaction to be strong possibilities that explain the circumstellar structure. The exotic nature of DFK 52 makes it a useful candidate to study major mass-loss events that can occur during the RSG phase, so we emphasise the need for future multi-wavelength studies of this object.

Acknowledgements. We thank the reviewer for their helpful comments on this letter. This paper makes use of the following ALMA data: ADS/JAO.ALMA#2023.1.01519, ADS/JAO.ALMA#2024.A.00018.S. ALMA is a partnership of ESO (representing its member states), NSF (USA) and NINS (Japan), together with NRC (Canada), NSTC and ASIAA (Taiwan), and KASI (Republic of Korea), in cooperation with the Republic of Chile. The Joint ALMA Observatory is operated by ESO, AUI/NRAO and NAOJ. We gratefully acknowledge the use of Director's Discretionary Time at ALMA under project ADS/JAO.ALMA#2024.A.00018.S. G.Q. would like to thank funding support from Spanish Ministerio de Ciencia, Innovación, y Universidades through grant PID2023-147545NB-I00.

References

- Boothroyd, A. I., Sackmann, I. J., & Ahern, S. C. 1993, *ApJ*, 416, 762
- Brinch, C. & Hogerheijde, M. R. 2010, *A&A*, 523, A25
- Bujarrabal, V., Castro-Carrizo, A., Alcolea, J., & Sánchez Contreras, C. 2001, *A&A*, 377, 868
- Davies, B., Figer, D. F., Kudritzki, R.-P., et al. 2007, *ApJ*, 671, 781
- Davies, B., Plez, B., & Petrault, M. 2022, *MNRAS*, 517, 1483
- De Beck, E., Andrews, H., Quintana-Lacaci, G., & Vlemmings, W. H. T. 2025, *A&A*, 698, A179
- Ediss, G. A., Carter, M., Cheng, J., et al. 2004, in *Fifteenth International Symposium on Space Terahertz Technology*, ed. G. Narayanan, 181–188
- Gómez, J. F., Niccolini, G., Suárez, O., et al. 2018, *MNRAS*, 480, 4991
- González-Fernández, C. & Negueruela, I. 2012, *A&A*, 539, A100
- Humphreys, R. M., Helmel, G., Jones, T. J., & Gordon, M. S. 2020, *AJ*, 160, 145
- Humphreys, R. M. & Jones, T. J. 2022, *AJ*, 163, 103
- Humphreys, R. M., Richards, A. M. S., Davidson, K., et al. 2024, *AJ*, 167, 94
- Hunter, T. R., Indebetouw, R., Brogan, C. L., et al. 2023, *PASP*, 135, 074501
- Justanont, K., de Jong, T., Helmich, F. P., et al. 1996, *A&A*, 315, L217
- Kamiński, T. 2019, *A&A*, 627, A114
- Kamiński, T., Steffen, W., Tyłenda, R., et al. 2018, *A&A*, 617, A129
- Khoury, T., Vlemmings, W. H. T., Tafuya, D., et al. 2021, *Nature Astronomy*, 6, 275
- Klencki, J., Nelemans, G., Istrate, A. G., & Chruslinska, M. 2021, *A&A*, 645, A54
- Lagadec, E., Verhoelst, T., Mékarnia, D., et al. 2011, *MNRAS*, 417, 32
- Marton, G., Gezer, I., Madarász, M., et al. 2014, *A&A*, 688, A203
- Moriya, T. J., Yoon, S.-C., Gräfener, G., & Blinnikov, S. I. 2017, *MNRAS*, 469, L108
- Negueruela, I., Marco, A., González-Fernández, C., et al. 2012, *A&A*, 547, A15
- O'Gorman, E., Vlemmings, W., Richards, A. M. S., et al. 2015, *A&A*, 573, L1
- Olofsson, H., Khouri, T., Maercker, M., et al. 2019, *A&A*, 623, A153
- Sahai, R., Huang, P. S., Scibelli, S., et al. 2022, *ApJ*, 929, 59
- Schneider, F. R. N., Ohlmann, S. T., Podsiadlowski, P., et al. 2020, *MNRAS*, 495, 2796
- Singh, A. P., Richards, A. M. S., Humphreys, R. M., Decin, L., & Ziurys, L. M. 2023, *ApJL*, 954, L1
- Tokuda, K., Fukui, Y., Harada, R., et al. 2019, *ApJ*, 886, 15
- Urquhart, J. S., Figura, C., Cross, J. R., et al. 2021, *MNRAS*, 500, 3050
- Wei, D., Schneider, F. R. N., Podsiadlowski, P., et al. 2024, *A&A*, 688, A87
- Yaron, O., Perley, D. A., Gal-Yam, A., et al. 2017, *Nature Physics*, 13, 510
- Zapartas, E., de Wit, S., Antoniadis, K., et al. 2025, *A&A*, 697, A167

Appendix A: Spectral energy distribution

We added the new ALMA 1.3 mm continuum flux and archival measurements from the Herschel/PACS point source catalogue (Marton et al. 2024) to the photometry compiled by Humphreys et al. (2020) to construct the SED for DFK 52 shown in (Fig. A.1). This reveals a double-peaked shape, with a cold dust component maximum at $\sim 70 \mu\text{m}$, yielding a temperature of $\sim 50 \text{ K}$. Although the spectral indices of the individual continuum components are unavailable with the current ALMA observations, a linear interpolation from the total ALMA flux to the PACS $120 \mu\text{m}$ yields an estimate of $\alpha \approx 3$, implying optically thin dust grains (O’Gorman et al. 2015) and supporting this assumption made in our dust estimates in Section 3.1.

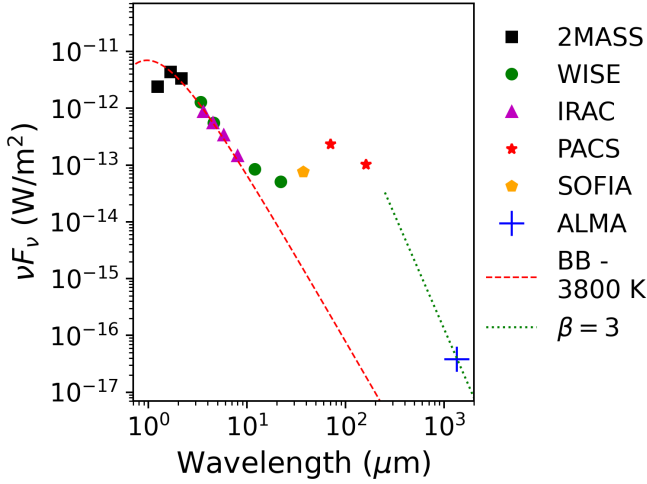


Fig. A.1. SED for DFK 52, including total ALMA flux measured in this work. Archival photometric measurements were corrected for foreground interstellar extinction by the same amounts as Humphreys et al. (2020). The lines are shown denoting the stellar blackbody (dashed red) as well as a spectral index of 3 extrapolated from the ALMA point (dotted green).

Appendix B: Details of the 3D radiative transfer model

In the two-component LIME model, the central component is treated as a spherically symmetric expanding wind with constant mass-loss rate. The extended component, similar to the set-up of Sahai et al. (2022), is modelled as an equatorial density enhancement (EDE) described as a 2D Gaussian in (spherical) radius and the z -coordinate:

$$n(r, z) \propto \exp\left(\frac{-(r - r_{\text{EDE}})^2}{2\sigma_{\text{EDE}}^2}\right) \times \exp\left(\frac{-z^2}{2h^2}\right). \quad (\text{B.1})$$

Here r_{EDE} is the radius where the density peaks, σ_{EDE} is the standard deviation of the enhancement, and the vertical scale height h is determined by the cylindrical radius coordinate R and an opening angle, θ_{EDE} :

$$h(R) = R \tan(\theta_{\text{EDE}}/2). \quad (\text{B.2})$$

The temperature profile for both structures is a power law in radius with log-slope $\alpha = 1$, based on the stellar temperature and radius. A minimum kinetic temperature, $T_{\text{min}} = 15 \text{ K}$, is also

needed because this power law reaches unphysically low values at large radii where the torus is found.

Due to the very different radial density dependences of the two components, populations were simulated separately using log r grid-sampling for the central component, and uniform sampling for the equatorial component. The excitation is collisionally dominated, and the observations indicate that the components do not overlap spatially at any velocity, so we do not expect the central and equatorial components to interfere with each other in optical depth or rotational populations. The parameters of the final RT model are included in Table B.1.

A comparison between the observed and modelled normalised line profile shapes is shown in Fig. B.1. We find that the fast EDE component and slow central component scale quite well to the total emission. While this suggests that material outside the equatorial regions may be comparable in its velocity distribution and optical depth properties, a full 3D model of the extended material is not yet possible due to the very high degree of geometrical complexity.

Parameter	Value
^{12}CO abundance w.r.t. H_2	2×10^{-4}
Stellar temperature, T_\star	3800 K ^a
Stellar luminosity, L_\star	$2.4 \times 10^4 L_\odot$ ^a
Temperature, T_{kin}	$T_\star \left(\frac{r}{R_\star}\right)^{-\alpha}$
Central component	
Mass-loss rate, \dot{M}	$3 \times 10^{-6} M_\odot \text{ yr}^{-1}$
Expansion velocity, v_{sph}	10 km s ⁻¹
Equatorial component	
Total mass, M_{EDE}	$0.05 M_\odot$
Expansion velocity, v_{EDE}	27 km s ⁻¹
Center radius, r_{EDE}	23000 au
Radial width, σ_{EDE}	6000 au
Opening angle, θ_{EDE}	10°

Table B.1. Physical parameters of the two-component RT model. ^aAdapted from (Humphreys et al. 2020).

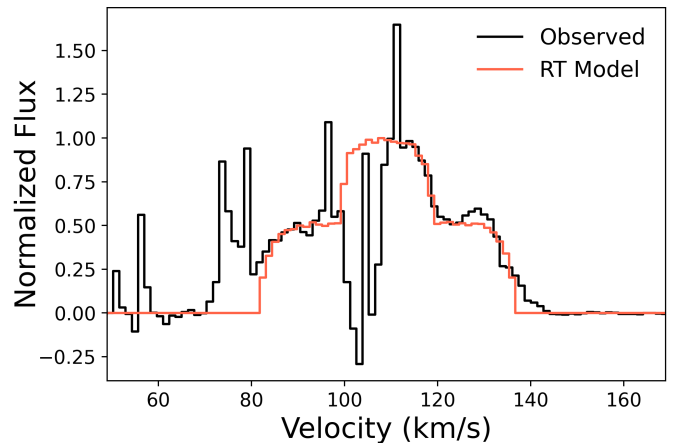


Fig. B.1. Observed ^{12}CO $J = 2 - 1$ line profile (black) and output of the two-component model (red). We note that normalised lines are used here to compare the shape of the emission, and that the RT model only accounts for 15% of the total observed flux.

Appendix C: Equatorial momentum analysis

The linear momentum estimated for the equatorial outflow, based on the derived parameters (see Table B.1), is approximately $2.7 \times 10^{38} \text{ g cm s}^{-1}$. To evaluate whether radiation pressure could account for this value, we computed the momentum it can deliver over the acceleration timescale using the formulation by Bujarrabal et al. (2001), $P = F \cdot P_{\text{rad}} = F \cdot L \cdot t_{\text{acc}}/c$, where the efficiency factor F describes the ability of dust to absorb and re-emit photons multiple times, enhancing momentum transfer. Assuming the current luminosity of $2 \times 10^4 L_{\odot}$ and an acceleration time of 1000 years—which corresponds to the duration of the ejection of the EDE—the resulting radiative momentum is $P_{\text{rad}} \approx 8.05 \times 10^{37} \text{ g cm s}^{-1}$ and the implied efficiency factor is $F \approx 3.35$.

In oxygen-rich massive post-AGB stars, the efficiency of momentum transfer from radiation pressure to the circumstellar gas is expected to be lower than in carbon-rich environments. This is primarily due to the reduced formation of carbonaceous dust grains, which are highly efficient at absorbing stellar radiation. Instead, oxygen-rich stars predominantly form silicate-based dust, which has lower opacity in the infrared, and thus couples less effectively with the radiation field. In environments with lower dust-to-gas ratios or less efficient dust species, this process is less effective and thus leads to reduced values of F . Additionally, in equatorial outflows, the geometry further limits the fraction of stellar radiation that can be redirected into the plane of the flow, so the F calculated above for DFK 52 must be considered a lower limit. As a rough estimate, for a torus height of 4000 au ($\approx 10^\circ$) and a radius of 23000 au, the EDE could intercept only about 9% of the total stellar radiation.

Bujarrabal et al. (2001) scaled the value of the effective opacity with the mass loss; their value of F is expected for mass losses of $\sim 10^{-4} M_{\odot} \text{ yr}^{-1}$. The average mass loss we obtained for the EDE is $\sim 5 \times 10^{-5} M_{\odot} \text{ yr}^{-1}$ ($=0.05 M_{\odot}/1000 \text{ yr}$). Thus, if we expect only 9% of the total of the photons to reach the region of the EDE and a $\tau_{\text{eff}} \sim 5$ times lower, we should reach (even assuming the same dust characteristics) a value of F of $9 - 17 \times 10^{-2}$, significantly smaller than the minimum efficiency derived. This supports the conclusion that an alternate ejection mechanism must be invoked to explain the formation of the EDE observed. If the equatorial component was indeed accelerated by radiation pressure, the stellar luminosity would have had to be 1–2 orders of magnitude higher than it is estimated now. Such a dramatic drop in luminosity over a timescale of a few 10^3 yr is not consistent with any predictions of single-star RSG evolutionary models (e.g. Zapartas et al. 2025); it is, however, consistent with the timescales and stellar parameter changes modelled for some merger products (e.g. Schneider et al. 2020).

Appendix D: Cluster membership

The interpretation of these data is reliant on the assumption that DFK 52 is a cluster member, and hence at the cluster distance of $5.8^{+1.91}_{-0.76} \text{ kpc}$ (Davies et al. 2007). If DFK 52 were in the background, its luminosity could be more in line with other extreme RSGs, but the size of the gas and dust emitting regions would cover even larger spatial scales than currently derived, further complicating the question of how such an envelope can be formed. On the other hand, if DFK 52 were in the foreground, the physical scales of emission would decrease; however, its luminosity would be even lower than currently quoted, challenging the star's classification as an RSG. In this case, the star would have a much later spectral type, due to the empirical relation-

ship between T_{eff} and CO band head strength for non-supergiants (González-Fernández & Negueruela 2012; Davies et al. 2007), and because the corrected SED would be substantially more reddened (Negueruela et al. 2012). A very evolved foreground AGB star could be considered, but even at a distance of 1.5 kpc (where the envelope size would be comparable to VY CMa), the luminosity would then be small even for AGBs ($< 2000 L_{\odot}$). The systemic velocity (109 km/s; measured with SiO) also lies comfortably within the cluster velocity range (100 – 120 km/s), and would be quite peculiar for a $d < 2 \text{ kpc}$ star, as the galactic rotation curve in this sight line predicts $v_{\text{lsr}} < 30 \text{ km s}^{-1}$ in that case. For these reasons, we argue for the current assignment that DFK 52 is indeed a cluster member, but a more accurate distance measurement is needed to confirm this.

Appendix E: ^{12}CO channel maps

The individual channel maps for ^{12}CO are shown in Fig. E.1. We find that emission on the redshifted side of the line is characterised by two prominent bubble-like shapes extending in the NE and SW directions, as well as the bar structure discussed in Sect. 3.2. In contrast, the blueshifted emission is more irregular, showing both smooth components as well as southward filamentary structures that do not converge to the stellar position at the highest relative velocities. Near the stellar velocity, the compact CO component appears, and we see bright emission from three confined clumps located at a radial distance of $1''$ (5800 au) from the stellar position.

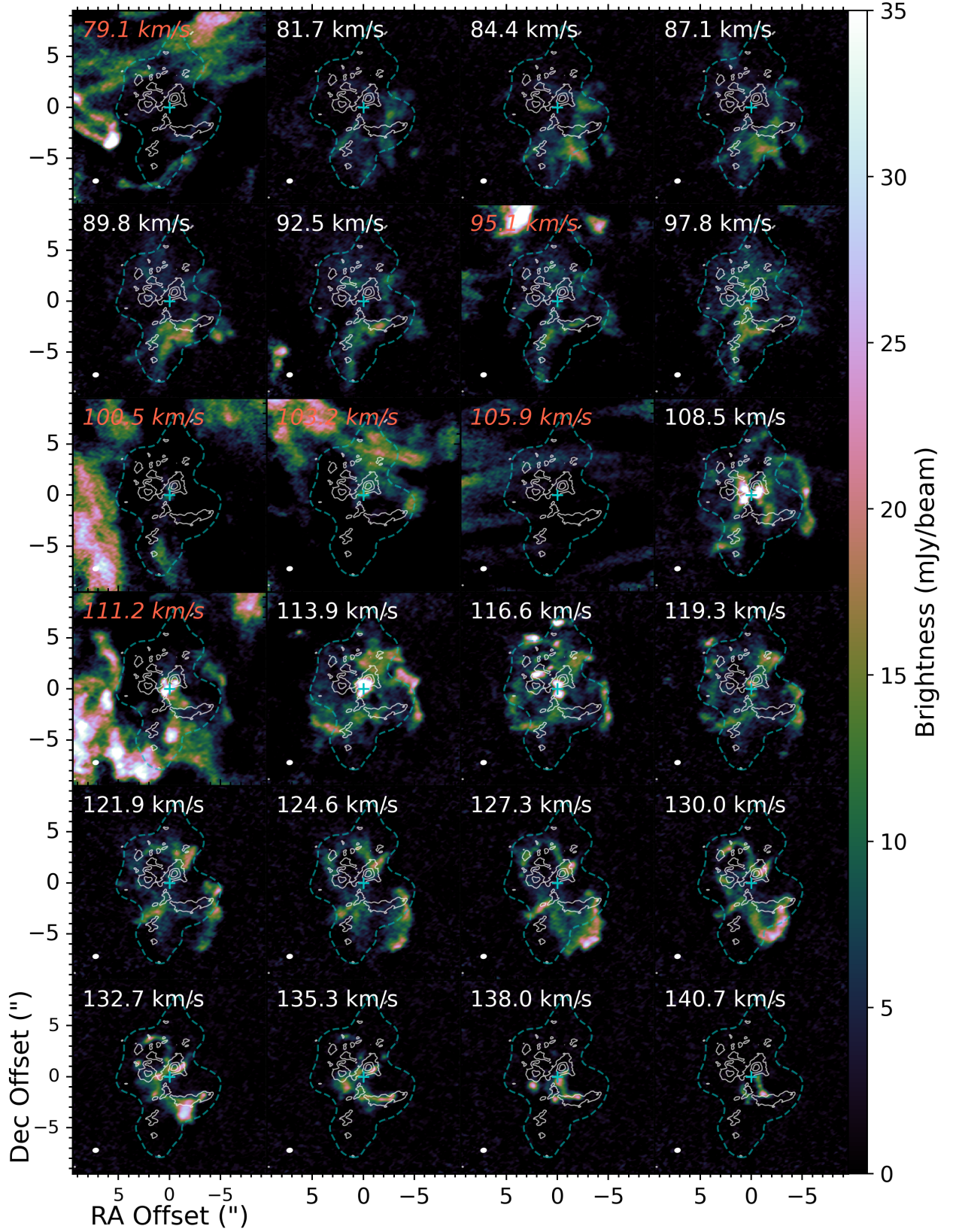


Fig. E.1. $^{12}\text{CO } J = 2 - 1$ channel maps. The systemic velocity is $v_{\text{sys}} = 109 \text{ km s}^{-1}$ and the channel width is 1.34 km s^{-1} . The white contours denote the 220 GHz continuum emission at 5σ , 10σ , and 15σ ; the blue dashed contours represent 3σ for the smoothed extended continuum component; and the blue cross marks the stellar position. The ALMA beam is shown in the bottom left of each panel (in white). The velocities written in red italics indicate channel maps that are heavily affected by ISM contamination.